

Supplementary Information for:

Functional Integration of Ni-Mo Electrocatalysts with Si Microwire Array Photocathodes to Simultaneously Achieve High Fill Factors and Light-Limited Photocurrent Densities for Solar-Driven Hydrogen Evolution

Matthew R. Shaner^{α,β}, James R. McKone^{α,‡}, Harry B. Gray^{ψ,α}, and Nathan S. Lewis^{ψ,α,β}

^ψBeckman Institute and Kavli Nanoscience Institute

^αDivision of Chemistry and Chemical Engineering

^βJoint Center for Artificial Photosynthesis

California Institute of Technology,

1200 East California Blvd, Pasadena, California 91125

E-mail: nslewis@caltech.edu

*To whom correspondence should be addressed

[‡]Current address: Department of Chemistry, Cornell University, Ithaca NY

I EXPERIMENTAL

Modeling

A zero-dimensional model was constructed to predict the maximum performance expected from the MEA-type photocathode device, based on a previously derived analytical expression for a buried junction in series with a catalyst and an additional resistor.¹ The expression was modified to produce Equation S1, where the γ factor (calculation shown in Equation S2) accounts for the additional junction area compared to the geometric (projected) area of illumination for a microwire array.^{2,3} Here n_d is the diode quality factor, k is Boltzmann's constant, T is the temperature in K, q is the unsigned charge on a single electron, J_L is the light-limited current density, $J_{0,PV}$ is the diode dark-current density, α is the catalytic charge-transfer coefficient (assumed to be equal for both forward and reverse directions), n_e is the number of electrons transferred, $J_{0,cat}$ is the catalyst exchange-current density, and R_s is the series resistance.

$$V(J) = \frac{n_d k T}{q} \ln \left(\frac{J_L - J}{\gamma J_{0,PV}} + 1 \right) + \frac{k T}{\alpha n_e q} \sinh^{-1} \left(\frac{J}{2 J_{0,cat}} \right) + J R_s \quad (S1)$$

$$\gamma \equiv \frac{\text{actual junction surface area}}{\text{projected surface area}} = \frac{\pi \times 1.9 \mu\text{m} \times 70 \mu\text{m}}{7 \mu\text{m} \times 7 \mu\text{m}} = 8.5 \quad (S2)$$

Table 1: Values used for the zero-dimensional model

Variable	Value
n_d	1.75
k	$1.38 \times 10^{-23} \text{ m}^2 \text{ kg s}^{-2} \text{ K}^{-1}$
T	298 K
q	$1.6 \times 10^{-19} \text{ C}$
J_L	$25 \text{ mA} - \text{cm}^{-2}$
γ	8
$J_{0,PV}$	$10^{-7} \text{ A cm}^{-2}$
α	0.5
n_e	2 electrons
$J_{0,cat}$	1.3 mA cm^{-2}
R_s	$2.6 \times 10^{-6} \text{ Ohm cm}^2$

Table 1 shows the values used for the parameters in the model. The light-limited current density, J_{ph} , was determined through two-dimensional full-wave simulations using a Maxwell's equations

solver (Lumerical) employing finite-difference time-domain algorithms.⁴ Each simulation consisted of a 60 μm tall and 2 μm diameter Si microwire loaded at the base by a layer of 200 nm diameter Ni-Mo particles at a mass loading of $\sim 1 \text{ mg cm}^{-2}$, covered by a layer of 200 nm diameter TiO_2 particles ($\sim 1 \text{ mg cm}^{-2}$). A two-dimensional, 7 μm wide, unit cell was used with Bloch boundary conditions on the sides, to simulate an infinite array as well as to yield transmissive top and bottom boundary conditions. Light was incident at an angle of 30 degrees. Single-wavelength simulations at 50 nm intervals from 350 nm – 1050 nm were performed and integrated using the AM 1.5G spectrum that had been binned to match the intervals at which the simulation data were computed. A 100 nm thick n^+ -Si emitter layer on the outer edge of the Si microwire was assumed to recombine all photoexcited carriers, and thus make no contribution to the J_{ph} value. The maximum J_{ph} value was calculated by summing all of the calculated photocurrent densities over the range of excitation wavelengths considered in the simulation.

The roughness factor, γ , was calculated for an array of 1.9 μm diameter and 70 μm tall microwires. The dark saturation-current density for the p-Si microwires with radial n^+ emitters, $J_{0,\text{PV}}$, grown by the vapor-liquid-solid growth method, was taken from the literature.⁵ The exchange-current density for the Ni-Mo catalyst, $J_{0,\text{cat}}$, was determined by modeling experimental data using the Butler-Volmer equation and by evaluation of the series resistance as determined by impedance measurements (Figure 3 in main text). The series resistance, R_s , was a general lumped circuit-element term that accounted for any additional resistances in the system. The sole contribution to R_s considered for this model was electron transport down the n^+ -Si emitter to reach the Ni-Mo catalyst deposited at the base of each microwire. The value of R_s was determined by assuming that all of the current flowed down the entire 70 μm length of the microwire, through a 200 nm thick emitter with a carrier concentration of 10^{19} cm^{-3} on a 1.9 μm diameter Si microwire.

Fabrication of Electrodes

Boron-doped ($N_A = 1 \times 10^{17} \text{ cm}^{-3}$) Si microwire arrays were grown via a Cu-catalyzed vapor-liquid-solid (VLS) process on B-doped (111)-oriented p-Si wafers (0.1–1 $\Omega\text{-cm}$ resistivity, Silicon Inc.).⁶ Three-inch diameter p-Si(111) growth wafers were received with a 500 nm thick thermal oxide (SiO_2) and were patterned photolithographically (MCC Primer and Shipley 1813

Microchem photoresist) using a mask with square pattern of 3 μm diameter holes on a 7 μm pitch. The exposed holes were etched through to the underlying Si by use of buffered hydrofluoric acid (BHF, Transene Inc.) for 5 min. 500 nm of Cu (EPSI 6N) was then thermally evaporated onto the wafer and the Cu was removed from everywhere but the 3 μm holes by lift-off in acetone. The wafer was diced to pieces that fit a 1" (OD) home-built chemical-vapor deposition (CVD) tube furnace, for microwire growth.

Si microwires were grown at atmospheric pressure using SiCl_4 (Strem, 99.9999+%) at 25 sccm flow rate, H_2 (Matheson, research grade) at 500 sccm flow rate, and BCl_3 (Matheson, 0.25% in H_2) at 1 sccm flow rate for 15 min. Following growth, the samples were cooled to ~ 200 $^\circ\text{C}$ under a 500 sccm flow of He. Microwire arrays were cleaned using a 6:1:1 (by volume) $\text{H}_2\text{O}:\text{HCl}$ (12 M, aqueous): H_2O_2 (9.8 M, 30 wt%) metal etch (RCA 2) for 20 min at 70 $^\circ\text{C}$. The samples were then subjected to a 15 s etch in BHF etch, a H_2O rinse, a 45 s etch with 5.4 M (30 wt%) KOH (semiconductor grade, Aldrich), and a H_2O rinse. A 100 nm thick SiO_2 layer was then grown via dry thermal oxidation for 100 min under an O_2 atmosphere in a tube furnace at 1050 $^\circ\text{C}$. The samples were then etched for 3 min in BHF to remove the oxide. This oxidation step is thought to getter Cu and other impurities from the core of the Si microwire, and etching of the oxide layer removes 50–100 nm of the metal-rich Si surface layer.⁶

Photoactive devices were made by forming phosphorus-doped n^+ -Si radial emitters and aluminum-doped p^+ -Si back surface fields on the p-Si microwire arrays and on planar, single-side-polished (111)-oriented p-Si wafers (Silicon Inc., 0.7 $\Omega\text{-cm}$). The substrates were first etched in BHF for 15 s, then rinsed with H_2O , and cleaned using a 5:1:1 (by volume) $\text{H}_2\text{O}:\text{NH}_4\text{OH}$ (aqueous): H_2O_2 (30% in H_2O) organic etch (RCA 1) for 20 min at 70 $^\circ\text{C}$. The samples were then etched in BHF for 15 s, rinsed with H_2O and cleaned using the RCA 2 metal etch for 20 min at 70 $^\circ\text{C}$. The samples were then etched in BHF for 15 s, rinsed in H_2O , dried in a stream of $\text{N}_2(\text{g})$, and the unpolished side of the sample was coated with 100 nm of aluminum by electron-beam evaporation. These samples were coated with a spin-on dopant (P509 Filmtronics) by spin coating at 2000 rpm for 30 s (Figure S1). The spin-on dopant was cured for 15 min at 200 $^\circ\text{C}$ on a hotplate in air. The samples were then annealed in a rapid thermal annealing (RTA) furnace under a 15 L min^{-1} flow of $\text{N}_2(\text{g})$ with the following process: a 20 s ramp to 880 $^\circ\text{C}$, a 30 s soak at 880 $^\circ\text{C}$, a 180 s linear cool to 820 $^\circ\text{C}$, and a cool to ~ 200 $^\circ\text{C}$ in a

flow of $N_2(g)$.⁷ In the RTA furnace, a 3" or 4" diameter Si wafer that had been coated once with spin-on dopant and cured was used as a holder for the samples. The planar and microwire samples were placed with the spin-on-dopant side facing downwards on the spin-on-dopant face of the Si holder wafer (Figure S2). This configuration allowed for gas-phase access of phosphorus dopants to any uncoated parts of the Si microwires from the Si holder wafer during the doping process. After cooling, the samples were etched in BHF for 3 min, rinsed with H_2O , and dried in a stream of $N_2(g)$. A porous underlayer (resulting from the spin-on dopant) that was not susceptible to etching in BHF remained near the microwire bases (Figure S3). To remove this residual material, an oxidation that consisted of a 10 min dry oxidation ($3\text{ L min}^{-1}\text{ O}_2$) at $800\text{ }^\circ\text{C}$, a 40 min wet oxidation at $800\text{ }^\circ\text{C}$ with Ar bubbling through $95\text{ }^\circ\text{C}$ water, and an additional 10 min dry oxidation at $800\text{ }^\circ\text{C}$, was performed. The warm up and cool down were performed under a 3 L min^{-1} flow of Ar. A final 3 min etch in BHF removed the residual defects, resulting in clean microwire and planar samples that were washed with H_2O and dried under a stream of $N_2(g)$ (Figure S4). Immediately prior to deposition of the catalyst/scattering layer, the samples were etched for 15 s in BHF, washed in H_2O , and dried in a stream of $N_2(g)$.

After the processing had been completed, ohmic contact was made to the Si substrates using an In-Ga (99.99%, Alfa-Aesar) eutectic that was scratched into the rear surface of the samples. Both Si and Ti foil substrates were affixed to a coiled Cu-Sn wire with Ag paint (SPI 05001-AB), with the Ag paint contacting the In-Ga on the Si substrates. The active area of the electrode was defined with epoxy (Loctite Hysol 9460), and the entire electrode was sealed with epoxy to the opening of a glass tube (6 mm outer diameter). The electrode orientation was determined by the orientation of the coiled wire that protruded from the glass tube. Geometric areas were measured by imaging the active area using a calibrated flat-bed scanner, and using software (ImageJ) to calculate the electrode area.

Synthesis and Deposition of Electrocatalysts

For synthesis and preparation of catalysts and photoelectrodes, all chemicals were used as received unless noted otherwise. Water was filtered using a MilliPore system and had a resistivity $> 18\text{ M}\Omega\text{-cm}$.

Ni-Mo nanopowder was synthesized following a previously reported procedure.⁸ Briefly,

an ammoniacal solution of nickel nitrate hexahydrate and ammonium molybdate containing a 3:2 ratio of Ni to Mo was mixed with diethylene glycol and heated rapidly to precipitate a mixed Ni-Mo oxide. The oxide was recovered and purified by consecutive washing and centrifugation first with water, then with acetone, and then with methanol, and was then dried in air. The resulting pale green powder was reduced under forming gas (5% H₂(g) in N₂(g)) at 400-500 °C for > 60 min to yield a black, pyrophoric Ni-Mo nanopowder. This powder was carefully suspended in isopropanol and the resulting colloid was used to generate catalyst inks.

The synthesis was slightly modified to produce Ni-Mo/C nanopowder, whereby the oxide was mixed with 20% by mass of carbon black (Vulcan XC72) and the mixture was thoroughly ground with a mortar and pestle. The subsequent reduction step was carried out as with the standard Ni-Mo nanopowder. The resulting carbon-composite powder was ~50% carbon content by mass and was significantly less pyrophoric than the pure Ni-Mo nanopowder.

Ni-Mo nanopowder was deposited on Ti foil electrodes and on Si photoelectrodes (both planar and microwire arrays) by centrifugal flocculation from the nanoparticle inks. The inks consisted of 1–2 mg mL⁻¹ of Ni-Mo nanopowder suspended in isopropanol with the addition of ~2% (by weight, relative to Ni-Mo) polytetrafluoroethylene (PTFE) particles from a water/alcohol suspension (Aldrich). The PTFE was added to increase the adherence of the nanoparticles to planar substrates. For deposition, the substrate was placed on a flat surface of polydimethylsiloxane (PDMS) in a centrifugation vial, and the appropriate amount of ink was added to achieve mass loadings of ~1 mg cm⁻². Prior to deposition, the ink was sonicated using a bath sonicator (Branson) for at least 30 min. The Ni-Mo/PTFE films were then flocculated by centrifugation at 3000 rpm for at least 5 min, after which the films were carefully removed and either air dried (planar samples) or manually dried by placing the films face-down on a paper tissue (Kimtech Kimwipe).

The PDMS/centrifugation-vial construct described above was produced by centrifuging the PDMS mixture overnight at 3000 rpm, which had the beneficial effects of removing air bubbles and producing a flat PDMS surface (Figure S5). Following deposition, the Si/Ni-Mo samples were annealed in forming gas for 30 min at 450 °C, but samples that contained Ni-Mo/C catalyst did not require this anneal.

TiO₂ nanoparticle suspensions were generated from hydrophobized TiO₂ pigment particles (DuPont TiPure R-105) suspended in isopropanol at a concentration of 100 mg mL⁻¹ of TiO₂ mass loading with 2% Nafion (by weight, relative to TiO₂; Aldrich). Deposition was performed in the same centrifugation vials as for Ni-Mo deposition, and consisted of drop-casting 15 μL of the TiO₂ ink and immediately centrifuging the electrode at 3000 rpm for several min. The Nafion was then cured by an anneal at 150 °C for 15 min in air. Initial experiments were performed with both hydrophobic and hydrophilic TiO₂ particles, with the hydrophobic particles showing superior performance (Figure S6).

Platinum particles were deposited electrolessly on Si substrates by use of a solution that consisted of 1 mM Pt and 2% HF in H₂O. Each electrode was etched for 15 s in buffered HF(aq) solution, washed, dried under a stream of N₂(g), and submerged for 1 min in the electroless Pt deposition bath. The electrode was then washed with H₂O, dried with a stream of N₂(g) and immediately tested to determine the photoelectrochemical behavior of the sample.

Characterization of Electrodes

Structural characterization of the various electrocatalyst deposits on Si electrodes was performed using a FEI Nova NanoSEM scanning-electron microscope. The current density vs potential behavior of the catalytic electrodes and photoelectrodes was measured using either a Gamry Reference 600 or a Biologic SP-200 potentiostat.

Electrochemical measurements were performed using either 0.5 M or 1.0 M trace-metal grade H₂SO₄ aqueous solutions (Fischer) as the electrolyte. Electrochemical experiments were performed in a two-compartment Pyrex cell that was equipped with a flat Pyrex window and with a Ag/AgCl reference electrode that was located in the same compartment as the working electrode. A Pt mesh or Ir/Ru/Ti oxide counter electrode was contained in a separate compartment that was isolated from the main cell compartment by a fine-porosity frit or by a Nafion membrane. All of the electrochemical data were collected with rapid stirring of the solution, to minimize mass-transport effects and to rapidly remove nucleated bubbles from the electrode surface.

The electrolyte was constantly bubbled with research grade H₂(g) (AirLiquide) to maintain a constant reversible hydrogen electrode (RHE) potential, as determined by measurement of the

open-circuit potential of a platinized Pt wire. The electrochemical potentials were adjusted to the RHE scale after data collection.

Electrodes were tested using cyclic voltammetry (CV) or linear-sweep voltammetry (LSV), at scan rates ranging from 5–20 mV s^{-1} , which were sufficiently slow to produce quasi steady-state behavior (validated by independent potentiostatic measurements). The current-density versus potential (J - E) data were not corrected for uncompensated resistance losses or for concentration overpotentials. Forward and reverse CV sweeps generally showed minimal hysteresis. When hysteresis was observed, the data collected while sweeping from negative toward positive potentials (reverse sweep) corresponded better to the steady-state polarization measurements, and thus were used for final analysis. LSV measurements generally were initiated at potentials that were several hundred mV negative of E_{RHE} , and were terminated at potentials just positive of where the electrode began to pass anodic current. This protocol effectively prevented the Si surface from oxidizing and minimized anodic stripping of the non-noble catalyst particles from the electrode surface.

The characteristics of the photoelectrodes were evaluated under simulated sunlight that was provided by a custom-built ELH-type tungsten-halogen light source or by a Xe lamp (Oriel 67005, Newport Instruments) equipped with an AM 1.5G filter (Newport Instruments 81094). The light source was placed at a distance from the electrochemical cell sufficient to generate an incoming photon flux above the Si indirect band gap (1.1 eV) equivalent to 1 Sun illumination, as measured by a Si photodiode (Thorlabs) that was calibrated relative to a NIST-traceable standard (Solarex).

The ideal regenerative cell efficiency (η_{IRC}) was adopted as the figure-of-merit for device performance.⁹ The value of η_{IRC} corresponds to the system efficiency of a two-electrode cell operating such that no net chemical reactions occur, in which the second, dark electrode is an ideally non-polarizable electrode performing the same reaction as the photoelectrode, but in the reverse direction. Equation S3 describes calculation of η_{IRC} , which is identical to the calculation of the efficiency of a photovoltaic cell. Here V_{mp} and J_{mp} are the voltage and photocurrent density at the maximum power point and P_{s} is the input solar power density; equivalently, V_{oc} is the open-circuit voltage, J_{sc} is the short-circuit current density and ff is the fill factor of the device.

$$\eta_{\text{IRC}} = \frac{V_{\text{mp}} \cdot J_{\text{mp}}}{P_{\text{s}}} = \frac{V_{\text{oc}} \cdot J_{\text{sc}} \cdot ff}{P_{\text{s}}} \quad (\text{S3})$$

Spectral-response measurements were performed using a custom-built apparatus. Monochromatic light with a bandwidth of 10 nm was produced using an Oriel monochromator and an Oriel Xe lamp. The beam was chopped at 20 Hz and was focused to a spot size that under-filled the sample. A mirror (10Q20BB.HR broadband dielectric mirror, Newport Corporation) was used to direct the horizontal beam vertically for the bottom-facing electrodes. The electrodes were tested in the same photoelectrochemical cell as described above for the measurements in 1.0 M KOH(aq). Each photoelectrode was maintained at -0.15 V versus RHE using a three-electrode set-up that was nominally identical to that used in the photoelectrochemical measurements described above, with a Biologic potentiostat (SP200) that was connected to a lock-in amplifier (SRS 830). A second lock-in amplifier was connected to a second photodiode that continuously monitored the light intensity provided by a portion of the incident beam that had been passed through a quartz beam splitter. Calibration of the light incident on the electrodes was performed using a bottom-facing calibrated photodiode (Newport FDS100-CAL) that was placed in the same location as the photoelectrode.

II RESULTS

Electrode Performance Statistics

Table S 1 summarizes a statistical analysis of the performance of nine n⁺p-Si/Ni-Mo/TiO₂ microwire electrodes and five n⁺p-Si/Pt planar electrodes. Insufficient quantities of all other electrode types limited the statistical analysis to these electrode types only.

Table S 1: Performance statistics for n⁺p-Si/Ni-Mo/TiO₂ microwire and n⁺p-Si/Pt planar electrodes.

Electrode Type	V_{oc} (mV)	J_{sc} (mA cm ⁻²)	ff	# of electrodes
n ⁺ p-Si/Ni-Mo/TiO ₂ Microwires	330 ± 52	7.7 ± 3.4	0.39 ± 0.28	9

n⁺p-Si/Pt Planar	550 ± 36	33 ± 4.8	0.59 ± 0.08	5
------------------------------------	----------	----------	-------------	---

As discussed in the main text and shown in Table S 1, the n⁺p-Si/Ni–Mo/TiO₂ microwire electrodes reproducibly exhibited lower performance as compared to the n⁺p-Si/Pt/TiO₂ microwire electrodes as well as with respect to the **best-performing** n⁺p-Si/Ni–Mo/TiO₂ microwire electrode **prepared in this work**. An effort to remedy this lower performance included eliminating the Ni–Mo activation annealing step by use of a carbon supported Ni–Mo electrocatalyst. This process succeeded in recuperating the open-circuit voltage, but different deposition characteristics lead to higher amounts of catalysts on the microwire sidewalls and thus lower light-limited current densities.

III SUPPLEMENTARY FIGURES

Figure S1 shows the base of a Si microwire array after the spin-on dopant (SOD) had been applied and cured. The position of the SOD is indicated relative to the Si microwire and relative to the SiO₂ mask used for microwire growth. A relatively thick layer (~700 nm) of SOD deposits in between each microwire covered the SiO₂ layer. The SOD coating thinned out to a non-uniform coating along the microwire sidewalls, with uncoated Si present in the dark regions. The absence of shorting, in conjunction with high V_{oc} values, suggests that these bare regions received sufficient dopant through vapor transport to form a high-quality emitter.

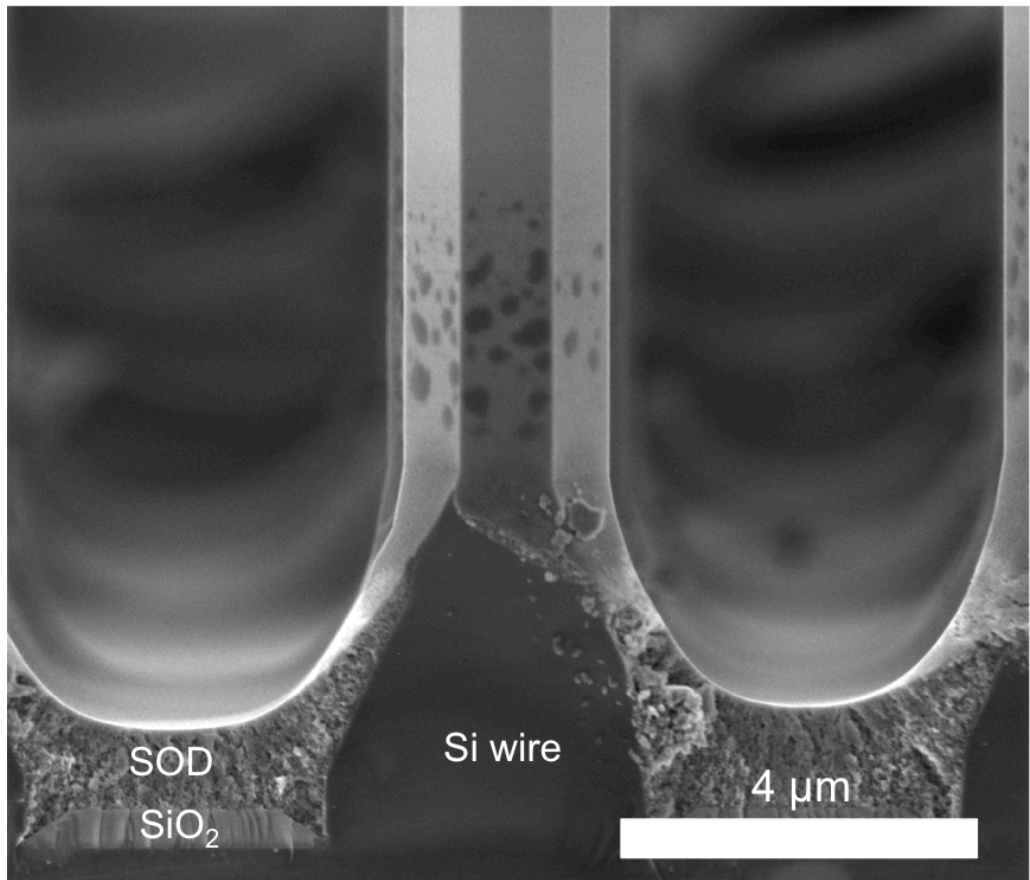


Figure S1: SEM image of the base of a microwire array that has undergone deposition and curing of a spin-on dopant (SOD).

Figure S2 shows schematically the process by which samples were annealed in a rapid thermal annealing (RTA) furnace to form the photoactive junction in both planar and microwire p-Si devices. This architecture was chosen to balance the amount of SOD material removed after annealing while providing sufficient dopant to form a high-quality junction. The handle wafer with SOD was used to provide supplementary dopant via vapor transport to the thin and non-uniform coating of SOD on the sidewalls of the microwires.

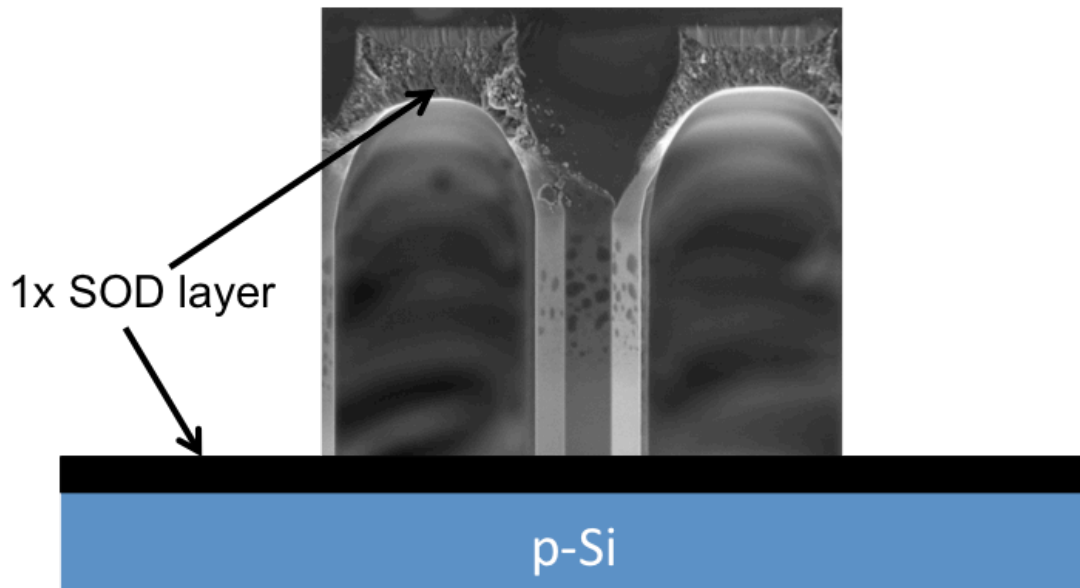


Figure S2: Schematic of the dopant drive-in process where a sample (planar or microwires) coated once by a spin-on dopant (SOD) is oriented within the rapid thermal annealing furnace with the SOD side face down on top of a handle wafer.

Figure S3 shows the residual material that remained after the prescribed HF treatment of the SOD post annealing. This material obscured light, caused catalyst-deposition challenges and reduced the height of the Si microwire available for light absorption.

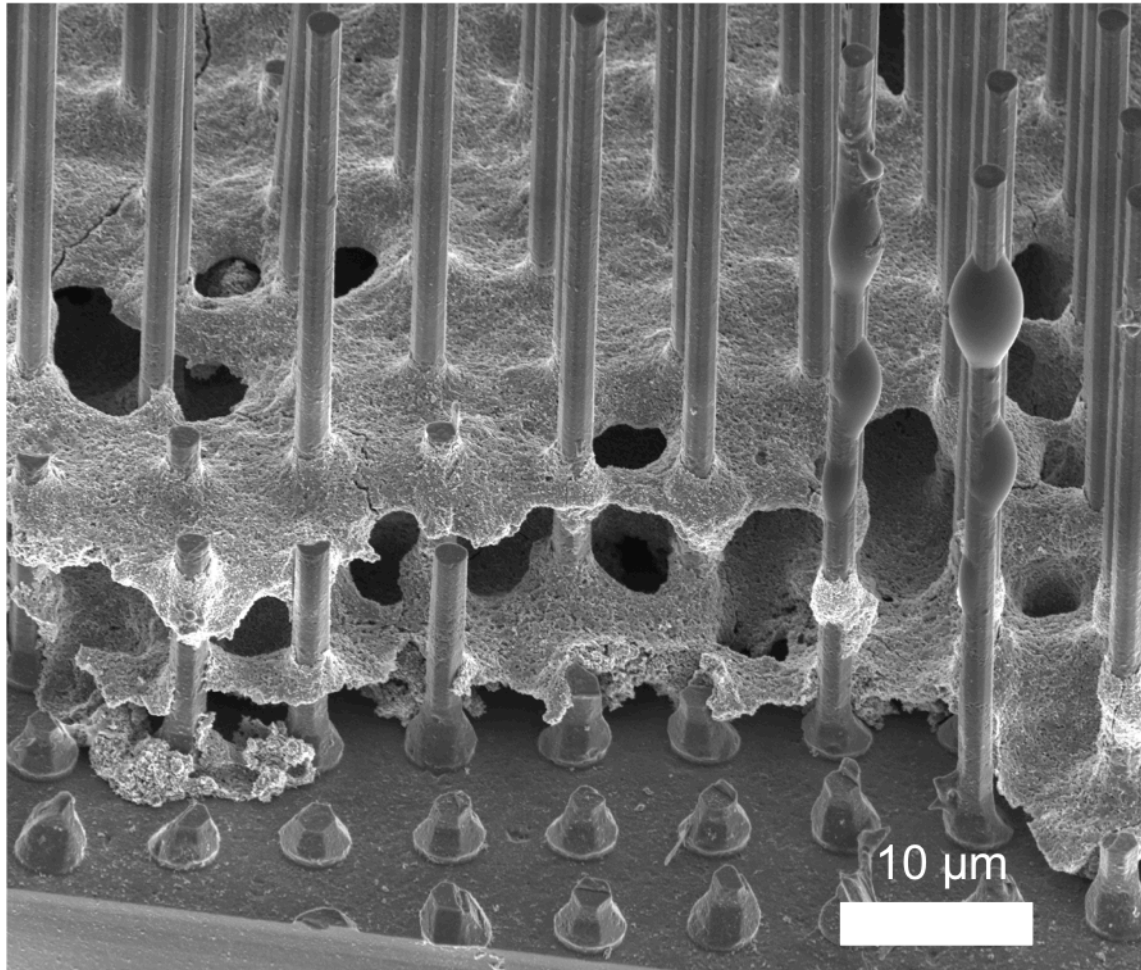


Figure S3: SEM image showing the spin-on dopant material remaining after the prescribed hydrofluoric acid treatment.

Figure S4 shows a clean n^+p -Si microwire array after a wet oxidation and HF etch to remove the residual SOD material depicted in Figure S3. The wet oxidation conditions were optimized to remove the residual material while maintaining a high-performance junction.

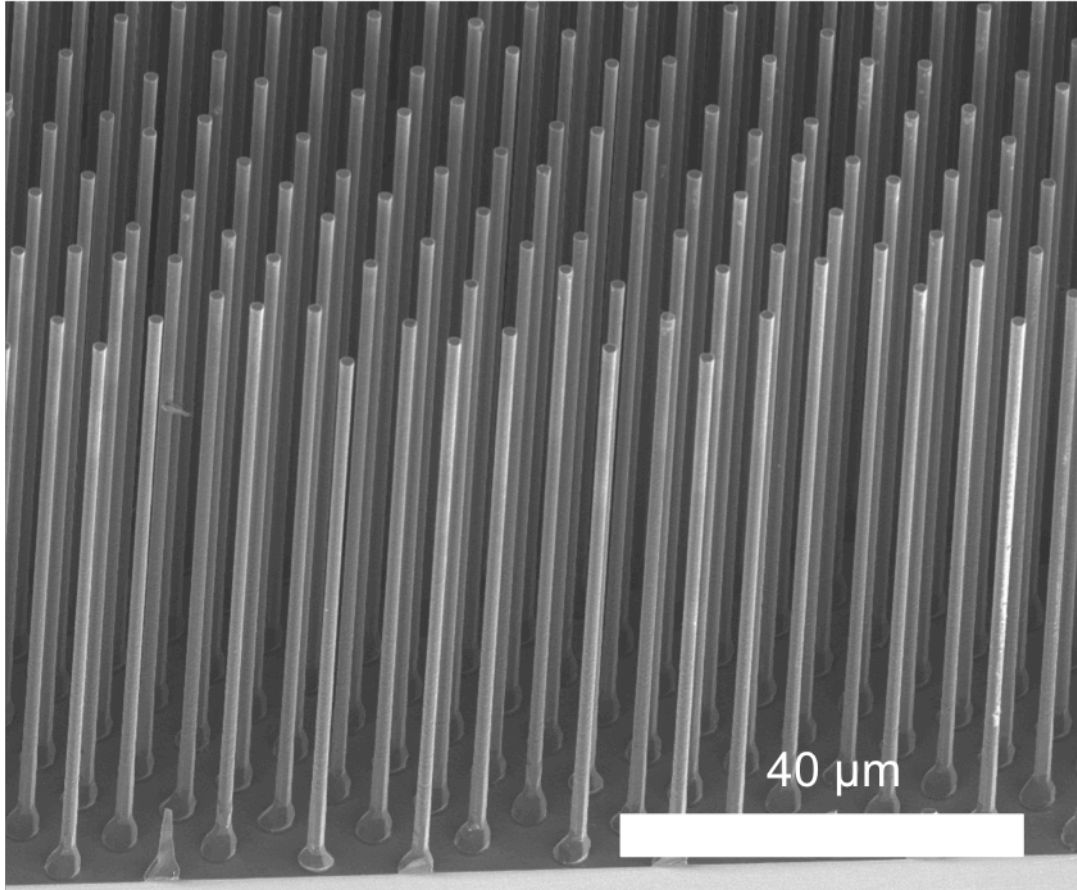


Figure S4: SEM image of a clean microwire array following a wet oxidation and HF etch to remove the residual spin-on dopant material. This sample was then ready for deposition of catalyst.

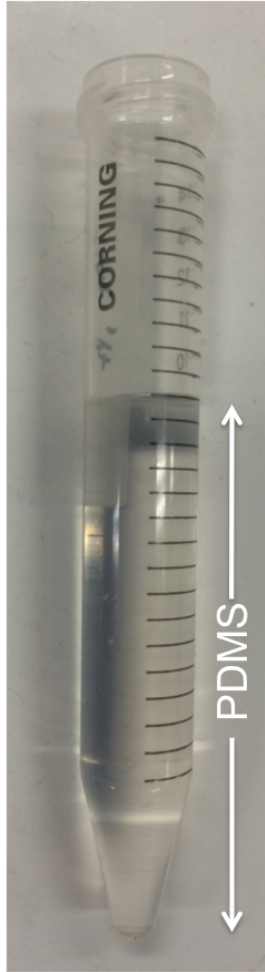


Figure S5: Centrifuge vial partially filled with PDMS to form a flat surface on which Si microwire samples were set for Ni–Mo and TiO_2 deposition. For TiO_2 , the small fluid volume was dropped directly onto a pre-placed Si microwire array and was centrifuged immediately thereafter.

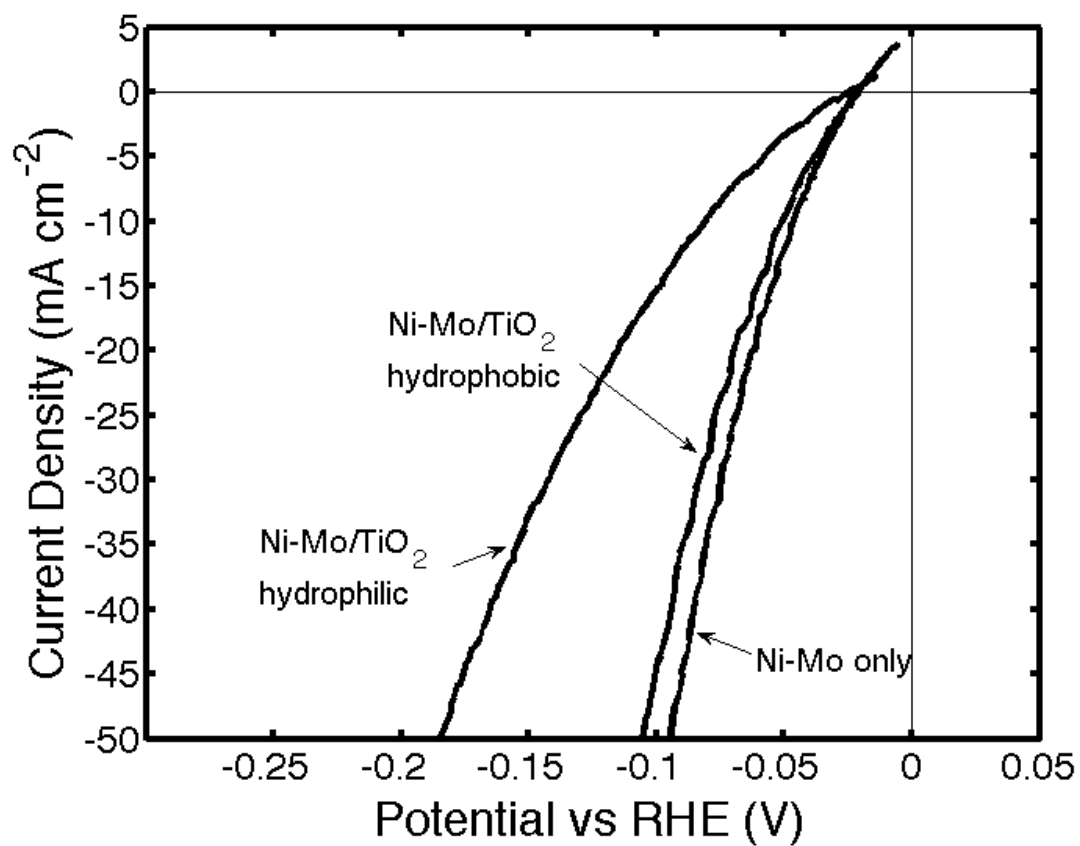


Figure S6: *J-E* hydrogen-evolution behavior of Ni–Mo catalysts on Ti foil with a coating layer of hydrophobic or hydrophilic TiO₂ particles. For reference, the performance of Ni–Mo catalysts without any TiO₂ coating is also shown.

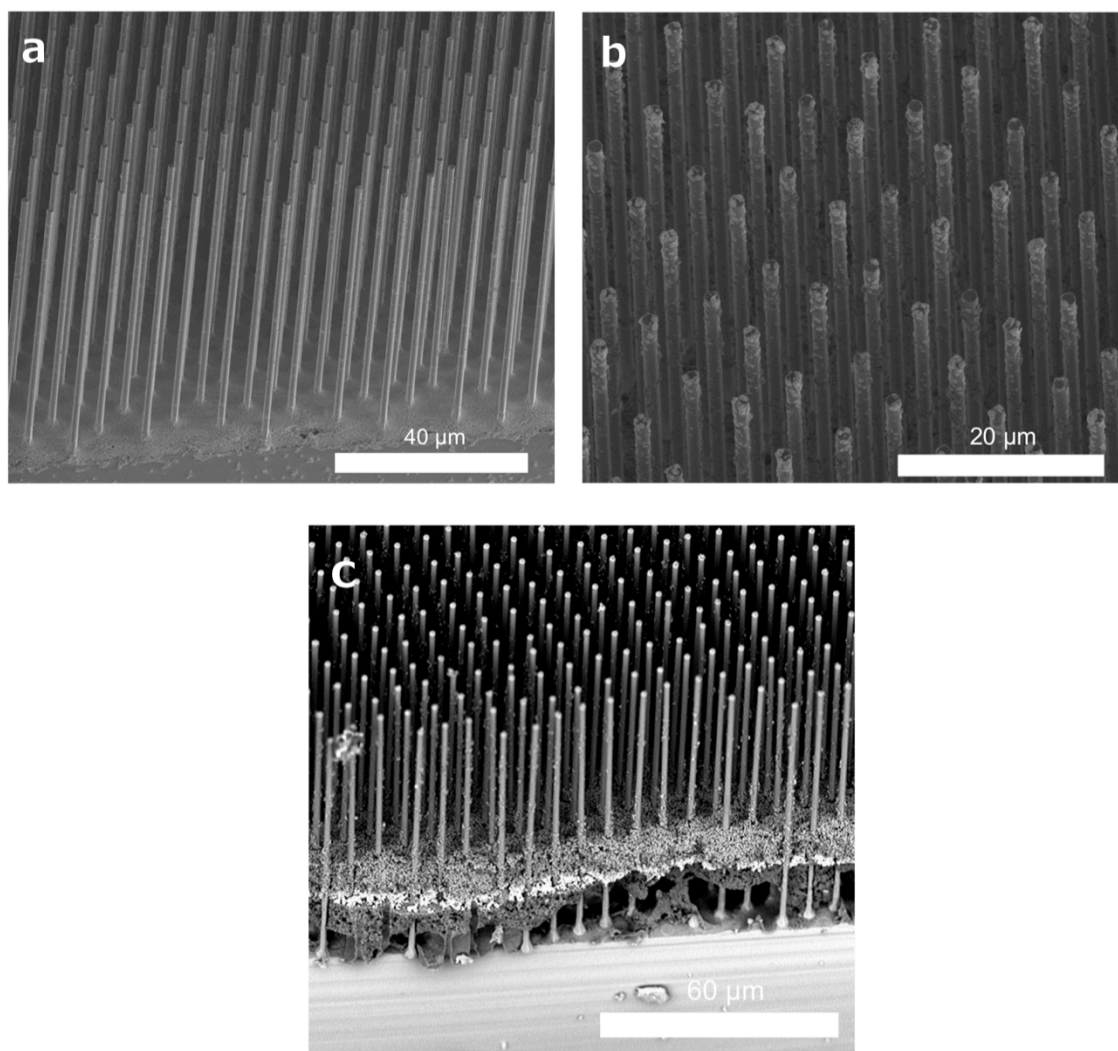


Figure S7: SEM images of the **best-performing** devices **prepared in this work**. a) Microwire array with a TiO_2 scattering layer only; b) Microwire array with a TiO_2 scattering layer as well as with electrolessly deposited Pt catalyst at the tops of the microwires; c) Ni-Mo/ TiO_2 /Si microwire array full MEA device.

Figure S8 shows a SEM image of catalyst and TiO₂ depositions that resulted in significant sidewall deposition. Such samples exhibited significantly reduced J_{ph} values relative to those reported in Table 2 (main text). Obtaining clean sidewalls required careful control of the drying process following centrifugal flocculation of the Ni–Mo catalyst layer. This behavior is consistent with small amounts of catalyst that remained in solution clinging to the Si sidewalls as the solvent front evaporated. This drying effect is similar to the well-known “coffee-ring” effect that results in inhomogeneous deposition of drop-cast particle suspensions.¹⁰ Additional efforts to carefully control the dynamics of flocculation and drying will likely yield reproducible catalyst layers without significant sidewall deposition.

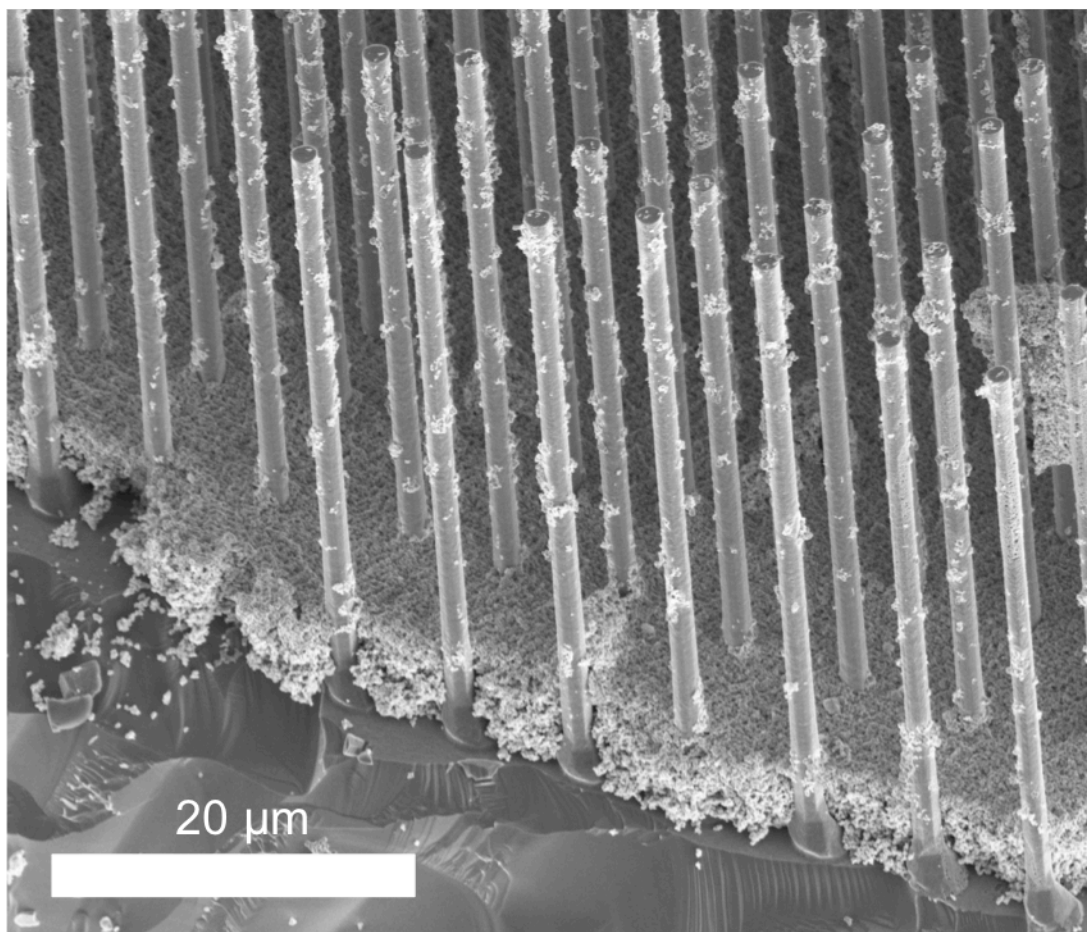


Figure S8: SEM image displaying an imperfect Ni–Mo deposition with much material on the microwire sidewalls. This causes increased parasitic light absorption by Ni–Mo and thus a reduced J_{sc} as compared to the **best-performing** device and modeling predictions **investigated herein**.

Figure S9 depicts the normal incidence absorption as a function of wavelength of four Si microwire samples with nothing (bare), Ni-Mo, TiO₂ and TiO₂/Ni-Mo layers, respectively. These absorption profiles were obtained by measuring each sample in reflection mode using an integrating sphere (Cary 5000) and assuming zero transmission due to the optically thick Si microwire growth substrate. Unambiguous identification of the source and photocurrent density contribution of the absorption for all samples is not possible with this data set alone because many absorbing components exist within each sample.

For the bare Si microwire sample, absorption occurs in the Si microwires and in the growth substrate. Ultimately, the desired device architecture includes the Si microwires removed from the substrate such that their absorption is the only useful absorption. For the TiO₂ sample a decrease in absorption is observed due to increased reflection. However, this overall decrease in absorption is not expected to result in a decrease in useful absorption in the Si microwires. Rather an increase in useful absorption is expected due to light scattering into the microwires rather than penetration into the growth substrate. This behavior is consistent a previous report.¹¹

The Ni-Mo sample has the highest absorption across all wavelengths because Ni-Mo is a good absorber in the UV thru near IR spectral region and the nanoparticles provide roughness in between the microwires as compared to the smooth surface in the case of the bare microwire array. The TiO₂/Ni-Mo sample has increased absorption as compared to the TiO₂ sample, which is consistent with Ni-Mo nanoparticles remaining on the microwire sidewalls and enhancing the long wavelength absorption.

For these reasons we have relied on the optical simulations and experimentally measured light-limited current density to provide an indirect measure of the light scattering effect, similar to a previous study that was directly focused on this concept.¹¹

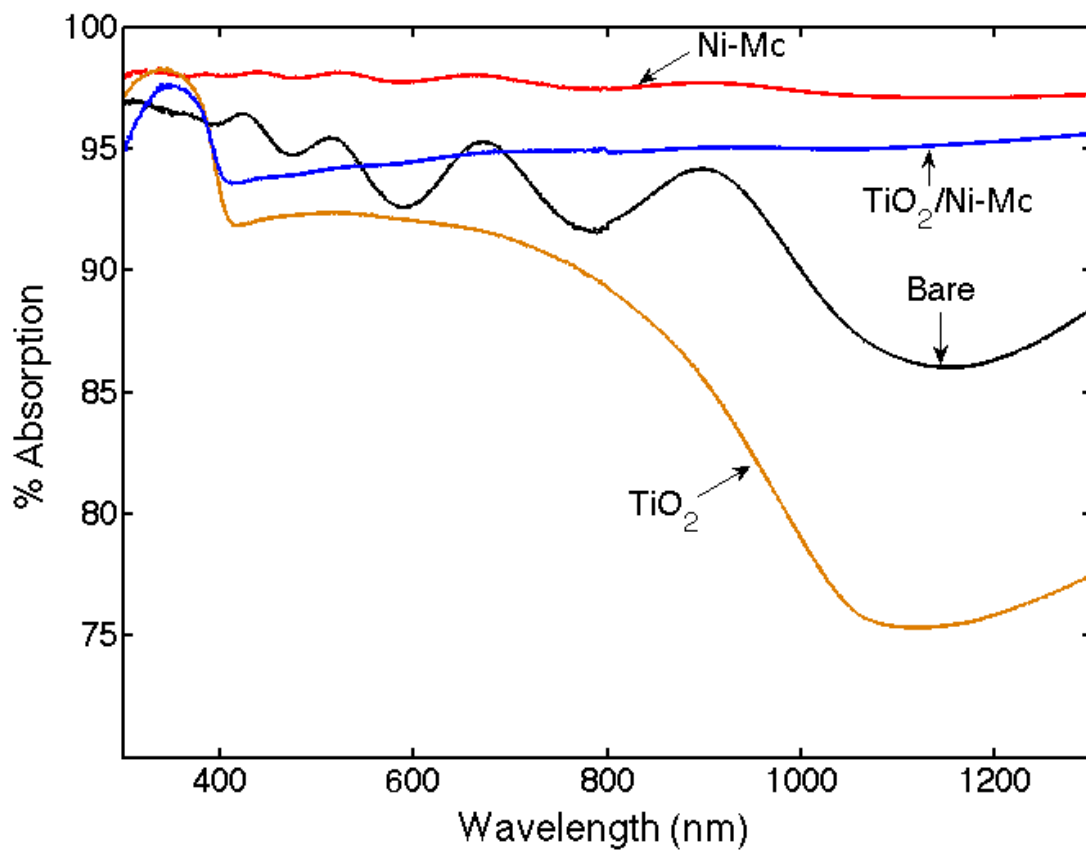


Figure S9: Absorption versus wavelength for four Si microwire samples with nothing (bare), Ni-Mo, TiO₂ and TiO₂/Ni-Mo layers, respectively.

Figure S10 and Figure S11 show SEM images of a Ni-Mo/TiO₂/Si microwire array after photoelectrochemical testing. These images demonstrate that the sample structure remains intact throughout electrochemical testing.

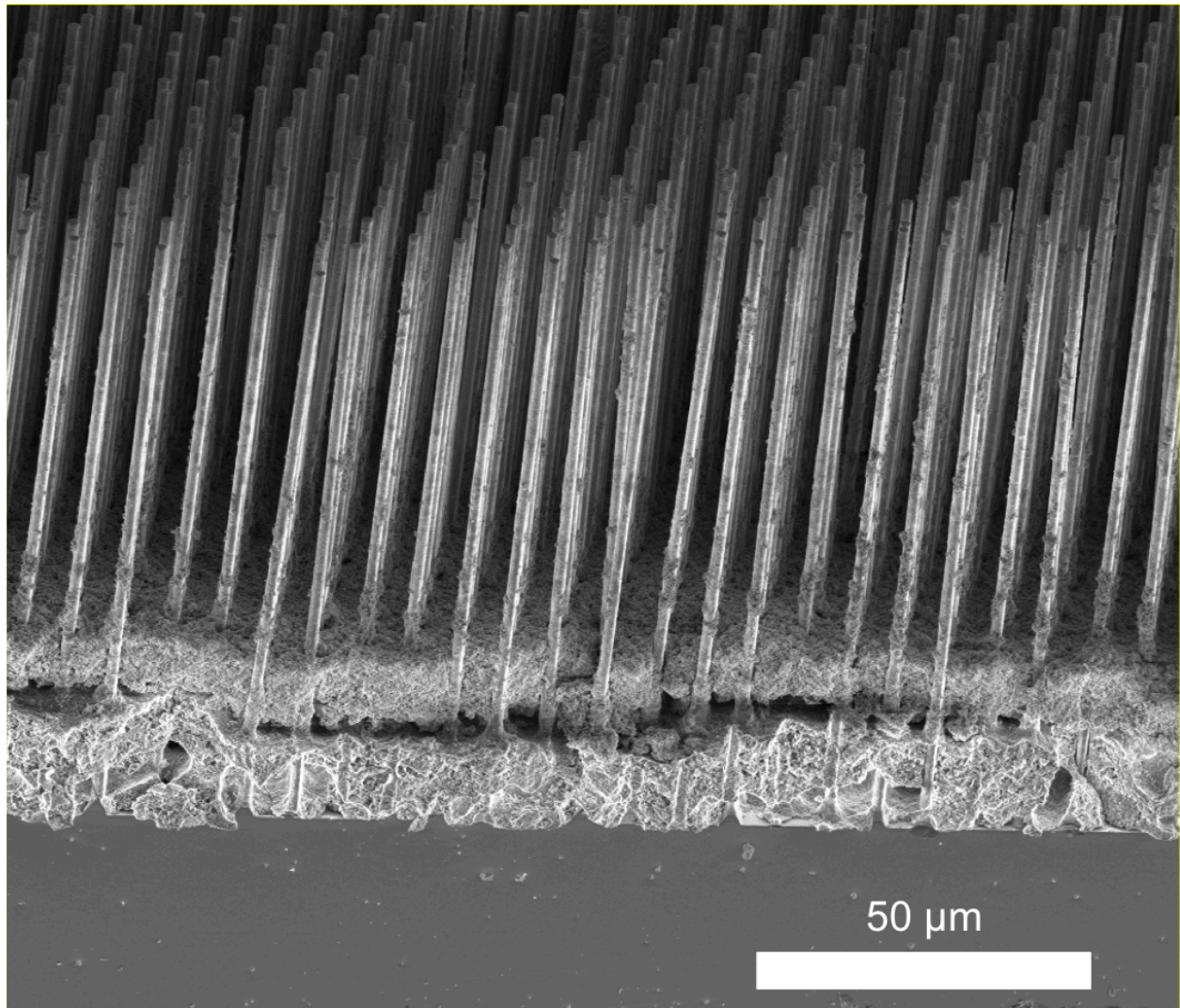


Figure S10: SEM image of a full wire array after PEC testing demonstrating the stability of the TiO₂/Ni-Mo layers.

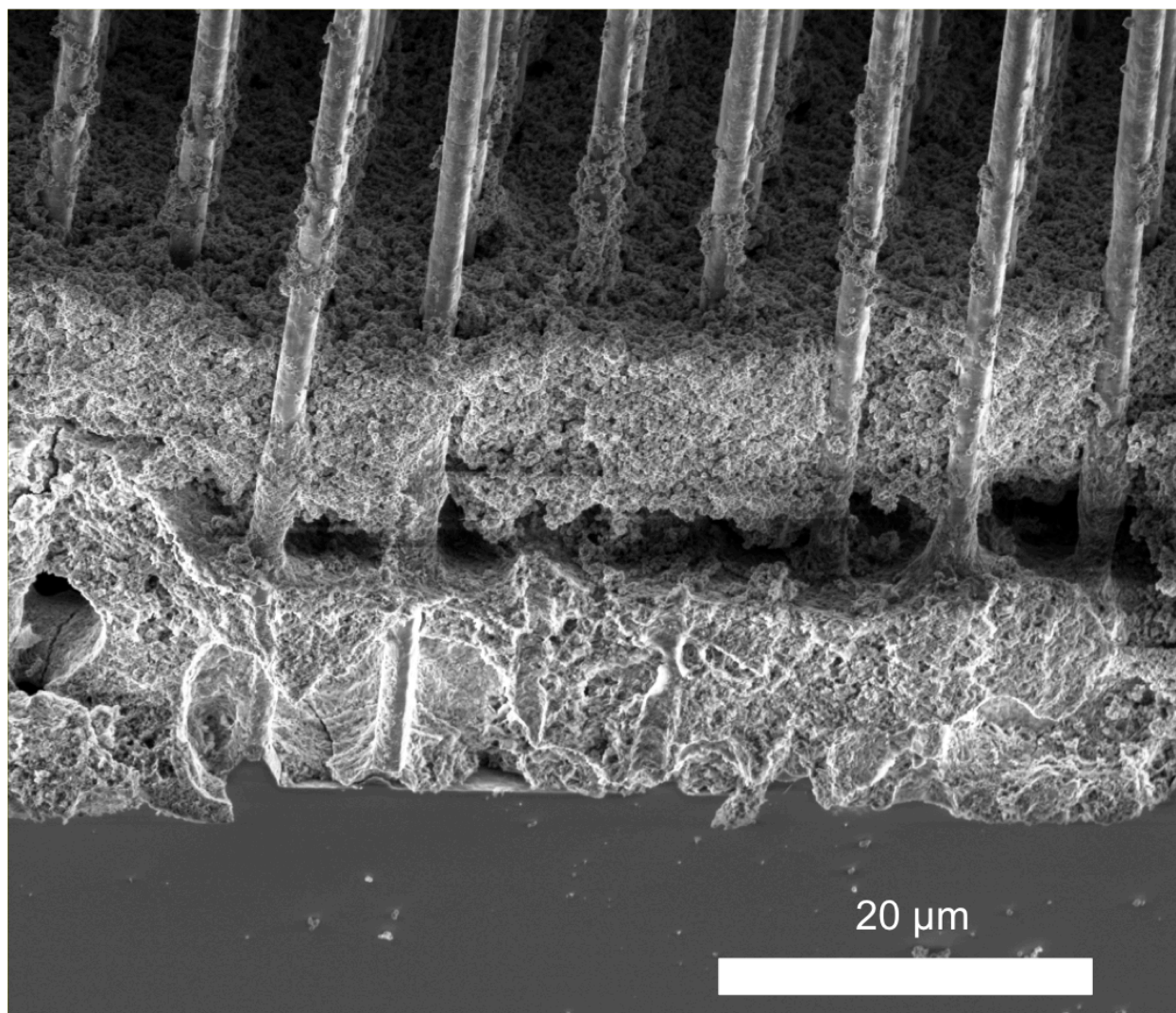


Figure S11: SEM image zoomed in on the layer structure after PEC testing demonstrating the stability of the $\text{TiO}_2/\text{Ni-Mo}$ layers.

III. SUPPLEMENTARY REFERENCES

1. M. R. Shaner, K. T. Fountaine, and H.-J. Lewerenz, *Appl. Phys. Lett.*, 2013, **103**, 143905.
2. B. M. Kayes, H. A. Atwater, and N. S. Lewis, *J. Appl. Phys.*, 2005, **97**, 114302.
3. J. M. Spurgeon, H. A. Atwater, and N. S. Lewis, *J. Phys. Chem. C*, 2008, **112**, 6186–6193.
4. M. R. Shaner, H. A. Atwater, and N. S. Lewis, 2012.
5. M. D. Kelzenberg, D. B. Turner-Evans, M. C. Putnam, S. W. Boettcher, R. M. Briggs, J. Y. Baek, N. S. Lewis, and H. A. Atwater, *Energy & Environmental Science*, 2011, **4**, 866.
6. S. W. Boettcher, J. M. Spurgeon, M. C. Putnam, E. L. Warren, D. B. Turner-Evans, M. D. Kelzenberg, J. R. Maiolo, H. A. Atwater, and N. S. Lewis, *Science*, 2010, **327**, 185–187.
7. A. Rohatgi, Z. Chen, P. Doshi, T. Pham, and D. Ruby, *Appl. Phys. Lett.*, 1994, **65**, 2087.
8. J. R. McKone, B. F. Sadtler, C. A. Werlang, N. S. Lewis, and H. B. Gray, *ACS Catal.*, 2013, **3**, 166–169.
9. R. H. Coridan, A. C. Nielander, S. A. Francis, M. T. McDowell, V. Dix, S. M. Chatman, and N. S. Lewis, *Energy & Environmental Science*.
10. R. D. Deegan, O. Bakajin, T. F. Dupont, G. Huber, S. R. Nagel, and T. A. Witten, *Nature*, 1997, **389**, 827–829.
11. M. D. Kelzenberg, S. W. Boettcher, J. A. Petykiewicz, D. B. Turner-Evans, M. C. Putnam, E. L. Warren, J. M. Spurgeon, R. M. Briggs, N. S. Lewis, and H. A. Atwater, *Nature Materials*, 2010, **9**, 239–244.